Available online at www.sciencedirect.com

SciVerse ScienceDirect

Acta Materialia 61 (2013) 217–227

Acta MATERIALIA

www.elsevier.com/locate/actamat

Plastic anisotropy and associated deformation mechanisms in nanotwinned metals

Zesheng You [a], Xiaoyan Li [b], Liangjin Gui [c,d], Qiuhong Lu [a], Ting Zhu [c,*], Huajian Gao [b,*], Lei Lu [a,*]

[a] *Shenyang National Laboratory for Materials Science, Institute of Metal Research, Chinese Academy of Sciences, Shenyang 110016, People's Republic of China*

[b] *School of Engineering, Brown University, Providence, RI 02912, USA*

[c] *Woodruff School of Mechanical Engineering, Georgia Institute and Technology, Atlanta, GA 30332, USA*

[d] *Department of Automotive Engineering, Tsinghua University, Beijing 100084, People's Republic of China*

Received 6 August 2012; received in revised form 12 September 2012; accepted 19 September 2012
Available online 17 October 2012

Abstract

Anisotropic plastic deformation in columnar-grained copper in which preferentially oriented nanoscale twins are embedded is studied by experimental testing, crystal plasticity modeling and molecular dynamics simulations. The dominant deformation mechanism can be effectively switched among three dislocation modes, namely dislocation glide in between the twins, dislocation transfer across twin boundaries, and dislocation-mediated boundary migration, by changing the loading orientation with respect to the twin planes. The controllable switching of deformation mechanisms not only leads to a marked dependence of yield strength on loading orientation, but also induces a strong orientation dependence of strain hardening that can be critical for retaining tensile ductility. These results demonstrate a new route for tailoring both nanostructure and loading to control the deformation mechanisms in order to achieve the desired mechanical properties in engineering materials.

Keywords: Nanoscale twins; Cu; Orientation effect; Anisotropy; Deformation mechanisms

1. Introduction

An overarching goal of engineering nanostructured materials is to achieve the desired combination of strength, ductility and work-hardening properties for particular applications [1–3]. Nanocrystalline materials usually exhibit high strength but their ductility and work hardening are limited because dislocation activities are suppressed by the tiny crystallites [2,4]. In contrast, nanotwinned face-centered cubic (fcc) metals exhibit a combination of high strength and moderate ductility and work hardening [5–10]. This has been attributed to a high density of randomly distributed twin boundaries (TBs) that restrict dislocation slip in a manner analogous to conventional grain boundaries (GBs) while retaining ample room for dislocation accumulation and plastic strain accommodation [5,6,11]. In equiaxial-grained nanotwinned Cu (nt-Cu) with ⟨110⟩ texture, it was demonstrated that the strength increases with decreasing twin thickness, as predicted by the well-known Hall–Petch model based on dislocation pile-up (the first deformation mechanism) [6]. However, when the twin thickness falls below a critical size, the strength is reduced by nucleation and motion of partial dislocations parallel to the twin planes (the second deformation mechanism) [12,13]. In Cu samples with preferentially oriented nanoscale twins, the movement of threading dislocations confined inside the twin lamellae could dominate the plastic deformation when the tensile

* Corresponding authors. Fax: +86 24 23998660 (L. Lu).
E-mail addresses: ting.zhu@me.gatech.edu (T. Zhu), huajian_gao@brown.edu (H. Gao), llu@imr.ac.cn (L. Lu).

1359-6454/$36.00 © 2012 Acta Materialia Inc. Published by Elsevier Ltd. All rights reserved.
http://dx.doi.org/10.1016/j.actamat.2012.09.052

axis is parallel to the twin planes (the third deformation mechanism) [14]. In spite of intensive study of deformation mechanisms in nanostructured metals, it is interesting to note that the above three dislocation-based deformation mechanisms have never been reported in the same material.

The TB orientation can be an essential factor governing the deformation behavior of nanotwinned metals. In contrast to normal GBs that impede dislocation movement, the coherent TBs allow dislocation glide within twin planes. TBs can also act as dislocation barriers as well as dislocation sinks, as revealed in detail by previous modeling [15–20]. With a change of TB orientation, the dominant effect of TBs on dislocation glide can vary, leading to TB orientation-dependent plastic response, i.e. anisotropic plasticity. However, a systematic experimental investigation on the anisotropic plastic behavior and properties of nanotwinned metals is still lacking, due in part to the difficulty of synthesizing bulk nanotwinned sample with preferentially oriented twins.

Plastic anisotropy is an important feature in laminate materials. For instance, in poly-synthetically twinned (PST) TiAl alloys [21–25], it was found that the yield stress of PST TiAl alloys with twin lamellae is strongly dependent on the loading orientation relative to the lamellar interfaces [21–23]. This type of plastic anisotropy was attributed to the activation of dislocations with different slip modes as dictated by the distinct and complicated microstructures with γ and α_2 phases in PST TiAl alloys [24]. Recently, Mara et al. [26] also showed that nanolaminate Cu–Nb pillars yield at a relatively low stress when compressed at 45° with respect to the interfaces. Most of previous studies focused on the orientation effect of incoherent interphase interfaces. Coherent twin interfaces in single-phase fcc metals present a uniquely interesting case, because the twin interfaces also act as slip planes of dislocations and provide ample room for dislocation storage [3].

In this paper, we show that a columnar-grained Cu with preferentially oriented nanotwins is an ideal candidate to probe the plastic anisotropy of nanotwinned metals. This was achieved by combining experiments, crystal plasticity modeling and massively parallel molecular dynamics (MD) simulations. Our work reveals that the three deformation mechanisms, i.e. dislocation pile-up, confined dislocation glide and partial dislocation-induced TB migration, could be controllably switched by tuning just one parameter, namely the orientation of TBs with respect to the loading direction. The results not only advance the understanding of the strengthening mechanisms in nanostructured metals, but also point to a new route for controlling and optimizing the mechanical properties for nanostructured metals.

2. Experimental procedure

High-purity Cu sheets with nanoscale growth twins were synthesized by means of direct-current electrodeposition from an electrolyte of $CuSO_4$. The procedure is described in detail in Ref. [14]. By carefully controlling the deposition parameters, nt-Cu sheet with highly aligned nanotwins was deposited to a thickness of ~1.5 mm, which enables the measurement of mechanical properties through normal compression testing along different directions with respect to the preferentially oriented TBs.

Compression samples with a cross-section area of $0.8 \times 0.8\ mm^2$ and a length of 1.2 mm were cut from the as-deposited Cu sheet using an electric spark machine and then mechanically ground to the desired dimension. To investigate the anisotropic mechanical properties, samples with their compression direction oriented at different angles (θ), including perpendicular ($\theta = 90°$), parallel ($\theta = 0°$) and inclined ($\theta = 45°$), with respect to the deposition plane (coincident with the twin planes which are preferentially oriented parallel to the deposition plane), were produced, as illustrated in Fig. 1.

Uniaxial compression tests at room temperature were performed on an Instron 5848 microtester with a 2 kN load cell at a strain rate of $1 \times 10^{-3}\ s^{-1}$. The cross-head displacement was used to determine the imposed strain, corrected for machine compliance. To minimize the friction between samples and platens, which had been polished to mirror finish, vaseline paste was used as a lubricant during compression tests.

Plan-view and cross-section view of microstructures of the as-deposited Cu specimens were examined by field emission gun scanning electron microscopy (SEM) in a FEI Nova NanoSEM 430 microscope with backscattering electron imaging. The samples were mechanically polished, then electropolished in a solution of phosphoric acid (25%), alcohol (25%) and deionized water (50%) at room temperature. To explore the deformation microstructure, cross-section observations of the samples compressed in different directions were performed by transmission electron microscopy (TEM) using a JEOL 2010 microscope with an accelerating voltage of 200 kV.

3. Atomistic simulation

We have performed large-scale atomistic simulations to study the interactions between dislocations and TBs in samples loaded in different directions with respect to TBs. Our results provide insights into the orientation effect of dislocation nucleation and propagation in nanotwinned metals; these findings complement the experimental work and the crystal plasticity modeling. The details of the atomistic simulation are described below.

The simulated sample consists of four columnar grains with a high density of nanotwins, as shown in Fig. 2. The mean grain size is about 50 nm, and the subgrain twins have a thickness of 5 nm. These characteristic sizes are directly scaled down from the experiments. The whole system contains 25.5 million atoms. The sample is $[1\,\bar{1}\,\bar{1}]$-textured, and four grains have in-plane orientations of 0°, 30°, 60° and 90° relative to a horizontal axis (i.e. the x-axis), so that all the GBs are of high-angle type. The system is initially

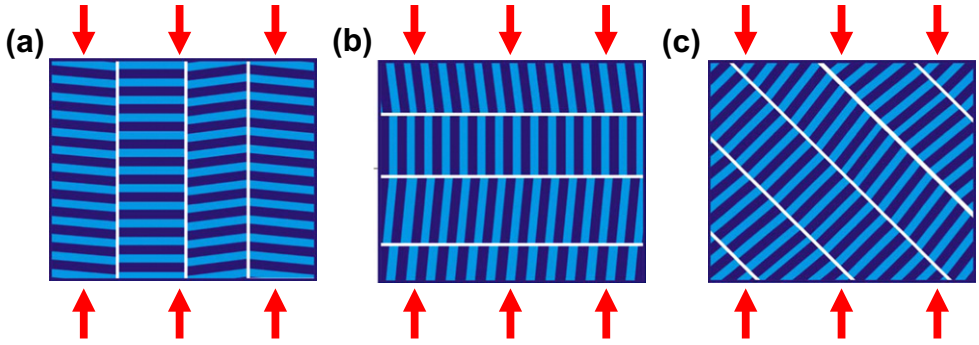

Fig. 1. Schematic diagram showing the uniaxial compression direction with respect to the TBs: (a) 90° compression; (b) 0° compression; (c) 45° compression.

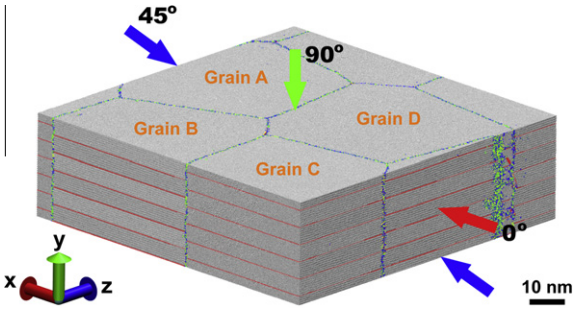

Fig. 2. Atomic configuration of the simulated samples. The directions of three loading modes (90° compression, 0° compression and 45° compression) are indicated by the green, red and blue arrows, respectively. Each columnar grain is also labeled by an orange index. The x, y, z axes within the matrix of grain A are oriented in the crystallographic directions $[1\,\bar{1}\,2]$, $[1\,\bar{1}\,\bar{1}]$ and $[1\,1\,0]$, respectively. Grains B, C and D are rotated counterclockwise along the $[1\,\bar{1}\,\bar{1}]$ direction (y axis) by 30°, 60° and 90°, respectively. Atoms are colored based on the local crystalline order. (For interpretation of the references to colour in this figure legend, the reader is referred to the web version of this article.)

equilibrated for 500 ps at 300 K and then subjected to three different loadings (illustrated in Fig. 2): (1) 0° compression, (2) 90° compression and (3) 45° compression. These loading conditions are accomplished through stepwise straining at a constant engineering strain rate of $2 \times 10^8\ s^{-1}$. Since the strain rate used in MD simulations is 10 orders of magnitude higher than that in experiments, the flow stresses from MD simulations are typically larger than those from experimental measurements.

For the 0° and 90° compression cases, the uniaxial loading conditions are realized by relaxing the simulation cell size in two other directions using the Berendsen barostat [27]. The 45° compression case is regarded as a combination of biaxial compression and pure shear. Throughout the simulations, periodic boundary conditions are applied in all three directions. We use the embedded atom method potential [28] to compute the interatomic forces, the Nosé–Hoover thermostat [29] to maintain constant temperature, and a multiple-time-step algorithm [30] for time integration. To visualize and identify defects during plastic deformation, we use the local crystalline order method [31] based on the following coloring scheme: grey for fcc atoms, red for hexagonal close-packed (hcp) atoms in TBs or stacking faults, green for atoms in dislocation cores or GBs, blue for atoms in the vicinity of vacancies, and yellow for fully disordered atoms. In addition, another coloring scheme (referred to as the position-based coloring) is used to generate 3-D effects, where the colors represent the distance of atoms from the center of the simulated grain.

4. Results and discussion

4.1. As-deposited nanotwinned copper

Fig. 3a shows a plan-view SEM image of the as-deposited sample, where numerous polycrystals are separated by clear and sharp GBs. The grain size exhibits a distribution from 1 to 6 μm with an average value of ~3 μm (see Fig. 4a). The cross-section SEM observation in Fig. 3b shows that these grains are columnar in shape and further subdivided into parallel nanoscale twin lamellae with most TBs parallel to the deposition plane. Statistics of twin thickness (i.e. λ, the spacing between two adjacent TBs) based on the TEM images reveals an average twin thickness of ~30 nm (see Fig. 4b). The electron backscatter diffraction (EBSD) analysis indicates that the as-deposited nt-Cu sample has a strong {1 1 1} out-of-plane texture, as shown in the inverse pole figure of the growth directions of the grains (the inset of Fig. 3a).

4.2. Anisotropic deformation behaviors

Fig. 5a shows the compression true stress vs. true strain curves of columnar-grained nt-Cu, which exhibit a strong dependence on loading direction. For Cu samples tested with the compression axis oriented at 90° and 0° with respect to TBs, the measured yield stresses are 598 ± 31 and 463 ± 16 MPa, respectively. Both samples exhibited only minor work hardening. In contrast, compression tests with the loading axis oriented at 45° to TBs result in a much lower yield stress of 230 ± 19 MPa, but accompanied by substantial work hardening. Evidently, Cu samples with preferentially oriented twins show strongly anisotropic plastic deformation behaviors in different loading

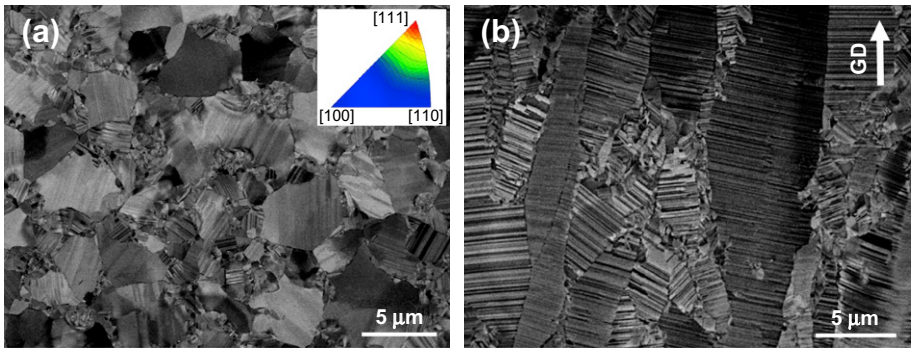

Fig. 3. SEM images of the as-deposited Cu sample. (a) Plan view. (b) Cross-section view. The images reveal that the sample is composed of micron-sized columnar gains with a high density of nanoscale twins. Most TBs are parallel to the deposition plane. The inset in (a) is the inverse pole figure of growth directions (GD) of the grains based on EBSD measurement, which shows the significant {1 1 1} out-of-plane texture.

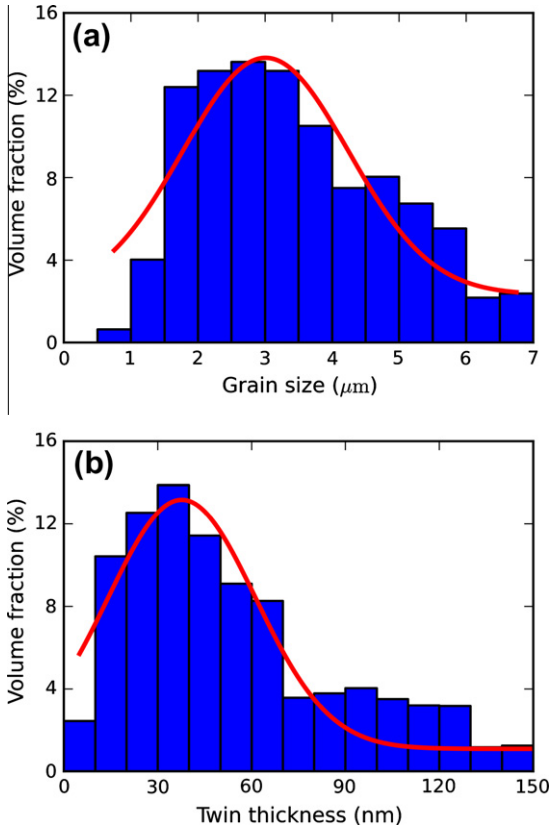

Fig. 4. Characterization of the representative specimen used in the experiments. (a) Histogram of grain sizes. (b) Histogram of twin thicknesses. The grain sizes in (a) are determined on the plan-view SEM images, while the twin thicknesses in (b) are from the cross-section TEM observations.

directions with respect to TBs. Fig. 5a also shows the stress vs. strain curves from the crystal plasticity modeling (Appendix A), which are in accord with experimental measurements.

The stress–strain curves from MD simulations of columnar-grained nt-Cu with a mean grain size of 50 nm and twin thickness of 5 nm are shown in Fig. 5b. The peaks of these stress–strain curves correspond to dislocation nucleation in the initially dislocation-free samples. Once there are enough dislocations to accommodate the imposed deformation, the stress drops to a characteristic lower level associated with the operative deformation mechanisms. Accordingly, we define the flow stress as the average stress beyond 7.5% strain, a level that sufficiently bypasses the initial stage of deformation controlled by dislocation nucleation. For 90° compression and 0° compression, the flow stresses are 2.646 ± 0.158 and 2.145 ± 0.083 GPa, respectively. In contrast, the flow stress is as low as 0.997 ± 0.136 GPa in 45° compression. Because of the short time scale accessible with MD, the sample is deformed at a high strain rate of $2 \times 10^8\ s^{-1}$. The calculated flow stresses are thus much higher than experimental measurements. For columnar-grained nt-Cu with a twin thickness of ~5 nm and a mean grain size of ~50 nm, the flow stress is experimentally measured to be higher than 1 GPa (see below), thus giving a difference by a factor of 2–3 due to the effect of ultra-high strain rates, consistent with previous MD simulations [32,33]. Clearly, the MD simulation results also confirm the strongly anisotropic plastic deformation behaviors of nt-Cu in different loading directions. The ratios of flow stress in Fig. 5b in 90° compression (σ_{90}) to that in 0° compression (σ_0) and in 45° compression (σ_{45}) are 1.23 and 2.65, respectively, which are quantitatively consistent with experimental values in Fig. 5a ($\sigma_{90}/\sigma_0 = 1.29$, $\sigma_{90}/\sigma_{45} = 2.6$).

The anisotropic mechanical behaviors of metals and alloys have been previously attributed to various causes, such as crystallographic texture [34], precipitates [35], latent hardening [36] and deformation-induced dislocation boundaries [37,38]. For the as-deposited nt-Cu without prior strain history, one possible explanation is the pre-existing {1 1 1} out-of-plane texture. However, the conventional Taylor model [39], which is useful in describing textural anisotropy [34], reveals a Taylor factor of 3.338 for 90° compression, 3.169 for 0° compression, and 2.987 for 45° compression based on the measured texture. This corresponds to stress ratios of $\sigma_{90}/\sigma_0 = 1.05$ and $\sigma_{90}/\sigma_{45} = 1.12$, which are much smaller than the experimental and simulation values. Therefore, the strong anisotropy in the yield stress and strain hardening in nt-Cu must be caused by other factors.

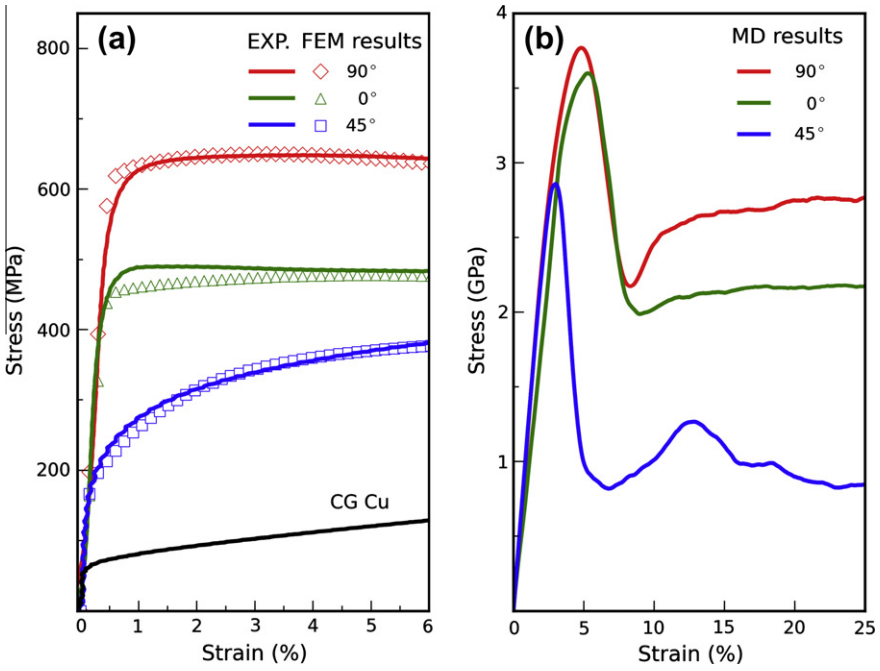

Fig. 5. Stress–strain curves for the columnar-grained nt-Cu with compression axis oriented at 90°, 0° and 45° with respect to TBs. (a) True stress–strain curves from experiment (lines) and finite-element method (FEM) simulation based on crystal plasticity modeling (symbols). (b) Stress–strain curves from MD simulations.

4.3. Hard vs. soft slip mode

To understand the origin of the strongly anisotropic yield stress and strain hardening, crystal plasticity modeling was conducted to determine the dominant active slip systems for each loading direction, as described in detail in Appendix A. Briefly, we employed a rate-dependent crystal plasticity formulation that explicitly accounts for plastic shearing rates on all the $\{111\}\langle 110\rangle$ slip systems. The dominant slip mode is then determined by the slip system with the largest plastic shearing rate. In addition, the measured stress–strain data for three loading orientations allow us to estimate the slip resistances as a function of shear strain on all the slip systems. These results show that the slip systems in nt-Cu can be classified into three categories: hard mode I (Fig. 6a-1, both slip plane and slip direction of the active slip systems, as well as the Burgers vector, are inclined to TBs), hard mode II (Fig. 6a-2, the slip plane is inclined to TBs but the slip direction is parallel to TBs), and soft mode (Fig. 6a-3, both the slip plane and slip direction are parallel to TBs). The slip resistances in both hard modes I and II are large, owing to the constraints of small twin spacing on dislocation glide. In contrast, the slip resistance in the soft mode is much lower, because of the weak constraint imposed by the relatively large grain size. Interestingly, each slip mode (i.e. slip system) dominates in one loading direction with respect to the TBs. That is, when the compression axis is perpendicular to the TBs (90° compression), the slip systems of hard mode I dominate. When the loading axis is parallel to the TBs (0° compression), the predominant slip systems belong to hard mode II. In the case of TBs aligned with the largest resolved shear stress (45° compression), the favorable slip systems are coplanar with the TBs and hence the soft mode with the least TB blocking prevails, leading to a low yield stress in the measured stress–strain curve.

Moreover, the loading orientation dependence of strain hardening can also be understood in terms of the hard and soft modes of slip. In the 45° compression case, the soft mode becomes dominant during deformation. Hence, the work-hardening capacity is controlled by the grain size that is relatively large, providing enough space within the grain to facilitate strain hardening through gradual accumulation of dislocations during deformation. On the other hand, the hard modes dominate for both 0° and 90° compression; in these cases, the strain hardening is largely suppressed due to the narrow spacing between adjacent TBs that limits the build-up of a high density of dislocations. Compared to the lamellar TiAl alloys, the marked anisotropy of strain hardening in nt-Cu arises due to the easy glide of dislocations on the coherent TBs, manifested by the frequent twinning/detwinning revealed by MD simulations and TEM observations as discussed below. Such a unique soft mode of deformation is enhanced by the nanosized twin lamellae that provide a high volume density of coherent TBs. It is important to emphasize that strain hardening is the dominant factor of retaining tensile ductility, which is a highly desired property for high-strength nanostructured metals. The variability of the strain-hardening behavior with different loading orientations in nanotwinned metals opens up possibilities of optimizing the strength and ductility by controlled arrangement of TB orientations. In contrast,

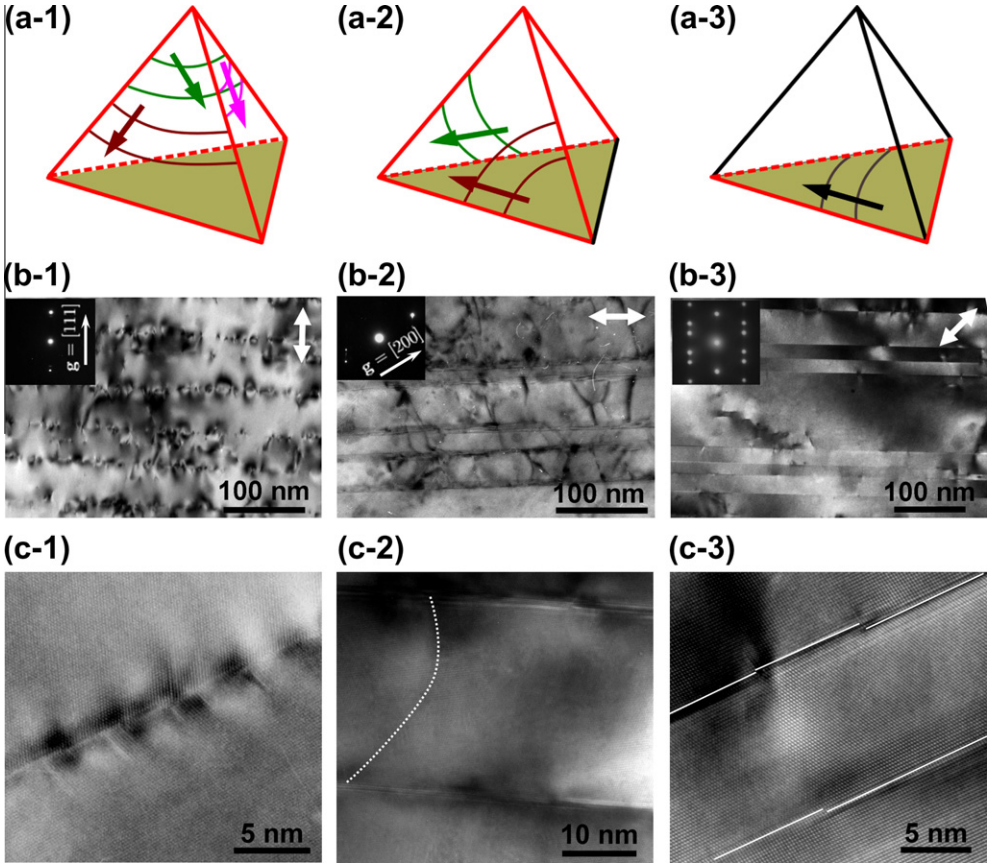

Fig. 6. Characteristic deformation processes in the columnar-grained nt-Cu with compression axis oriented at 90°, 0° and 45° with respect to TBs. (a) Schematic diagrams illustrating the active slip systems for the three compression directions: (a-1), 90°; (a-2), 0°; (a-3), 45°. (b) TEM and (c) HRTEM observations of the microstructure of samples in different loading directions: (b-1, c-1) 90° compression with a strain of ~5%; (b-2, c-2) 0° compression with a strain of ~6%; (b-3, c-3) 45° compression with a strain of ~7%. To reveal the dislocation types more clearly, tilting experiments were carried out, and b-1 and b-2 are bright-field images under two-beam conditions with $g = [1\,1\,1]$ (normal to TBs) and $g = [2\,0\,0]_M$, respectively.

the accommodation of plastic strain across the interfaces in laminate materials (e.g. boundaries across the lamellar γ and α2 phases in TiAl alloys) can be severely limited, thus reducing the strain-hardening capability and causing the easy fracture along the interfaces. This represents another important difference between the nanoscale twin-induced plastic anisotropy in pure metals and that in traditional laminate composites and alloys.

4.4. Atomistic dislocation mechanisms

MD simulations were used to probe the atomic-level dislocation activities related to the orientation dependence. Fig. 7 reveals the strained atomic configurations of the simulated samples at the same strain level of 9.34% but under different loading modes. Under 90° compression, dislocation traces remain short due to the blocking effects of TBs, whereas the dislocations extend much longer along TBs for the cases of 0° and 45° compressions. The active slip systems (including the slip plane and the Burgers vector) identified in the matrix of four grains under 90° compression, 0° compression as well as 45° compression are consistent with results from the crystal plasticity modeling.

Fig. 8a shows the details of dislocation structures at a compressive strain of 5.82% normal to TBs. In this case, most dislocations are nucleated from the GBs in the initial stage and glide on the inclined {1 1 1} slip planes until they finally pile up against TBs, indicating that TBs are strong barriers to dislocation glide (see Supplementary Movie S1). As the deformation proceeds, the dislocations start to cut through the TBs when the shear stress driving the incident dislocations is sufficiently large (see Figs. 7a and 9a). This trend agrees with previous MD simulations showing dislocation pile-up against and interaction with TBs [40–43] as the dominant deformation mechanism under straining perpendicular to TBs. Numerous dislocation debris accumulated along the TBs can be seen from the post-mortem TEM observation of the sample with 90° compression in Fig. 6b-1. The high-resolution TEM (HRTEM) image in Fig. 6c-1 confirmed that those dislocations bear the footprints of dislocation pile-up and slip transmission at the TBs, which is consistent with the dynamic processes revealed by the MD simulations. These results provide direct evidence of TB obstruction to dislocation glide as a major strengthening mechanism, as designated by hard mode I (Fig. 6a-1).

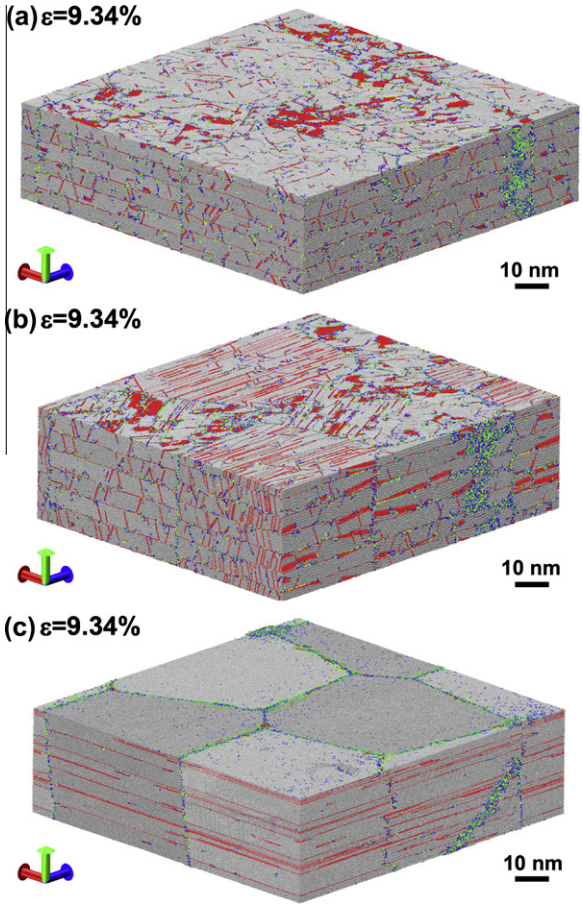

Fig. 7. Strained atomic configurations of the simulated sample under different loading modes: (a) 90° compression; (b) 0° compression; (c) 45° compression. In (a), dislocations cut through TBs. Their traces remain short due to the blocking effects of TBs. In (b), threading dislocations are fully confined in the twin or matrix lamellae. Threading segments span over the whole twin or matrix regions, while leaving behind long traces of misfit segments on TBs. In (c), dislocations are nucleated at TB–GB intersections and then glide on twin planes, leading to TB migration which changes the twin lamella thickness. Atoms are colored based on the local crystalline order. (For interpretation of the references to color in this figure legend, the reader is referred to the web version of this article.)

When the loading direction was changed to be parallel to the TBs, MD simulations revealed that the GBs were still the favorable dislocation nucleation sites. However, in contrast to the 90° compression, much less dislocation pile-up and slip transfer across TBs were observed (see Supplementary Movie S2). Instead, the dominant plastic deformation mechanism became propagation of individual dislocations along the inclined slip planes under the constraint by adjacent TBs, as shown in Figs. 7b and 9b. This resulted in threading segments spanning individual twin or matrix lamella with misfit segments lying in the TBs. These dislocations have hairpin-like loop configurations, as shown in Fig. 8b. Such threading dislocation structures that span the twin lamellar channel observed in post-mortem TEM/HRTEM observations (Figs. 6b-2 and c-2) are rather different from those observed in the 90° compression case. Detailed analysis shows that the Burgers vectors of

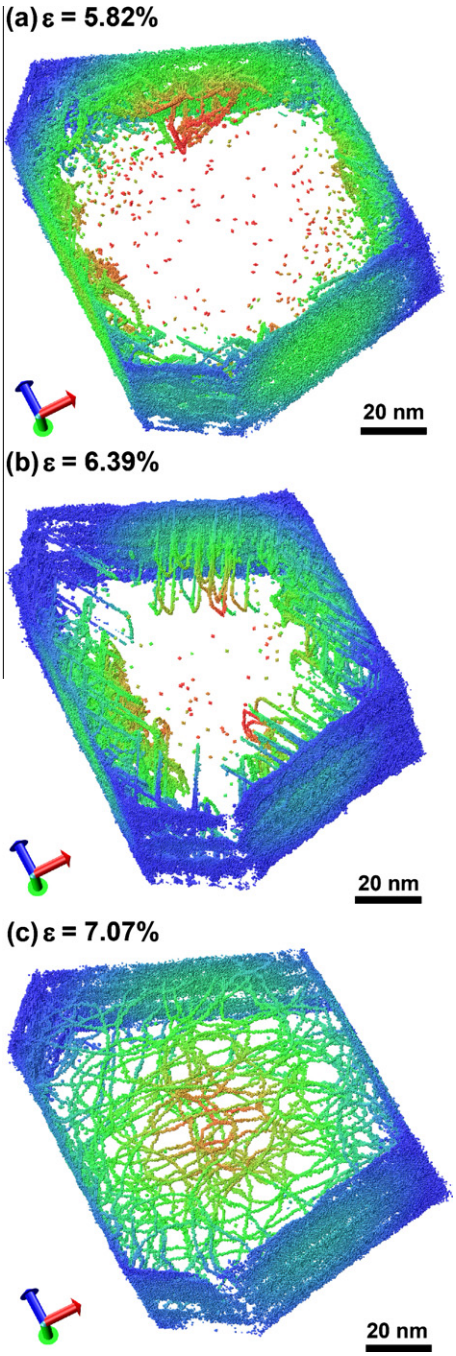

Fig. 8. Dislocation microstructures revealed by MD simulations: (a) dislocation pile-up and slip across TBs at a strain of 5.82% under 90° compression; (b) threading dislocations nucleated from GBs and gliding in the twin/matrix lamellae at a strain 6.39% under 0° compression; (c) partial dislocation gliding parallel to TBs and the induced TB migration at a strain of 7.07% under 45° compression. Dislocation structures are rendered in the position-based coloring.

the threading dislocations are parallel to the TBs, corresponding to the active slip systems of hard mode II (Fig. 6a-2). In the initial stage, the dislocations traveled far into the grain interior. As the applied strain increases, more dislocations gradually accumulate in the vicinity of

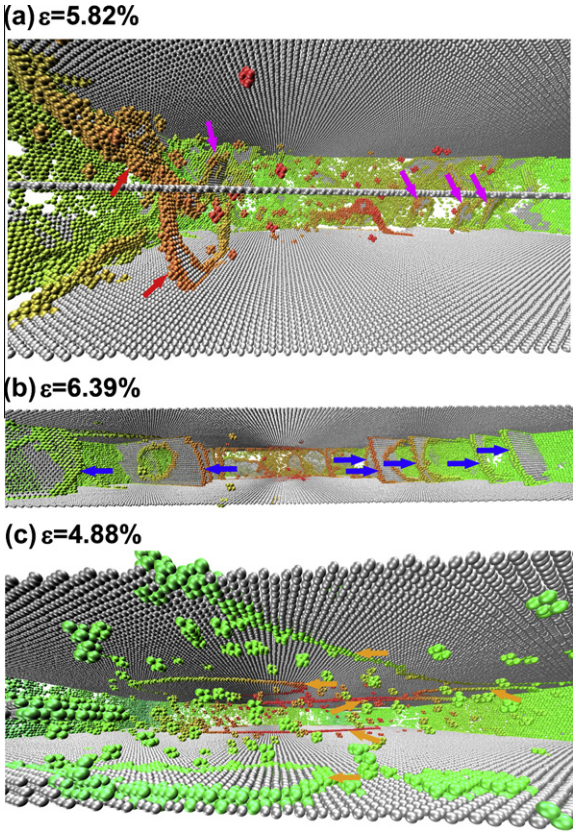

Fig. 9. Dislocation patterns in the representative grains under different loading modes: (a) 90° compression; (b) 0° compression; and (c) 45° compression. Herein atoms are painted by the position-based coloring. The silver atoms have hcp order, so single silver layers represent TBs, and double silver layers stand for the staking faults. In (a), dislocations nucleate at the TB–GB intersections and glide on the slip planes inclined to TBs, as pointed out by purple arrows. Dislocation cutting through the TB is marked by red arrows. In (b), threading dislocations nucleate from GBs, and then slip in the confined twin/matrix, as pointed by blue arrows. In (c), partial dislocations marked by orange arrows nucleate at the TB–GB junctions, and slip on the TBs.

GBs, and the GB-affected zone would take much larger plastic strain than that sustained by grain interiors [14].

For the case of 45° compression, the resolved shear stress is maximized on the twin plane, facilitating the activation of the soft-mode slip (Fig. 6a-1). Shockley partial dislocations, nucleated predominantly from the intersections between TBs and GBs, glide on the twin planes, as shown by MD simulations in Fig. 8c (also see Figs. 7c and 9c, and Supplementary Movie S3). The successive motions of these partial dislocations lead to TB migration, which thickens or narrows the twin lamellae depending on the direction of the partial dislocation in the twin plane. TEM observations (Fig. 6b-3) revealed fewer dislocations inside the twin lamellae, in contrast to a relatively higher density of stored dislocations between the TBs in the 90° and 0° cases. This difference is an intuitive consequence of the predominant motion of dislocations on the twin planes but not inside the twin lamellae as revealed by MD simulations (Fig. 8c). Many Shockley partial dislocations with Burgers vector parallel to the twin plane (manifested as steps on TBs) are clearly seen in Fig. 6c-3. The coupled partial dislocation motion and TB migration have also been demonstrated to play a key role in the plastic deformation of nanotwinned metals in experiments [44,45] and simulations [13,46,47], especially when the TBs are oriented with high Schmid factors [42,43]. It should be emphasized that the high mobility of dislocation in the TBs plays an essential role in the enhanced work hardening under 45° compression, which is in distinct contrast to other lamellar structures.

Fig. 10 shows evolution of defects as the applied strain increases under different loading modes in MD simulations. In Fig. 10a, the dislocation nucleation rates are much higher under 90° compression and 0° compression than that under 45° compression. In Fig. 10b, most of the dislocations under 0° compression are threading/channeling dislocations, and some of them are partials which leave behind numerous stacking faults spanning the twin/matrix lamellae. For 90° compression, a large number of extended dislocations are nucleated from the intersections between TBs and GBs, and then slip across TBs. The stacking faults between leading and trailing dislocations become narrow due to the blocking effects of TBs on the leading partials. Therefore, the number of hcp atoms in the case of 0° compression is greater than that for 90° compression. For 45° compression, twinning partial dislocations are nucleated at the TB–GB junctions and slip on the TBs, giving rise to TB migration and variation in twin lamella thickness. However, such activity does not change the number of hcp atoms before two neighboring TBs annihilate. The increasing number of hcp atoms is caused by partial dislocation nucleating from GBs and gliding on the slip plane parallel to TBs, leaving behind large areas of stacking faults.

4.5. Switchable deformation mechanisms and size dependence

Our combined experimental and modeling research at different scales provides new insights into the deformation mechanisms of nanotwinned metals. Firstly, there are three distinct dislocation-based deformation mechanisms in highly oriented nt-Cu. These three mechanisms, in conjunction with the conventional dislocation–dislocation interaction, constitute the dislocation-based deformation mechanism map in terms of the loading direction (θ) with respect to TBs and the average twin thickness (λ), as schematically shown in Fig. 11. When λ is larger than 100 nm, the intra-twin dislocation–dislocation interaction, which is insensitive to the loading direction, controls the deformation. However, as λ is reduced below 100 nm, the dislocation nucleation process and the enhanced interactions between dislocations and TBs make possible the active operation of different dislocation mechanisms under different loading directions. Secondly, it can be clearly seen from Fig. 11 that the three deformation mechanisms can be

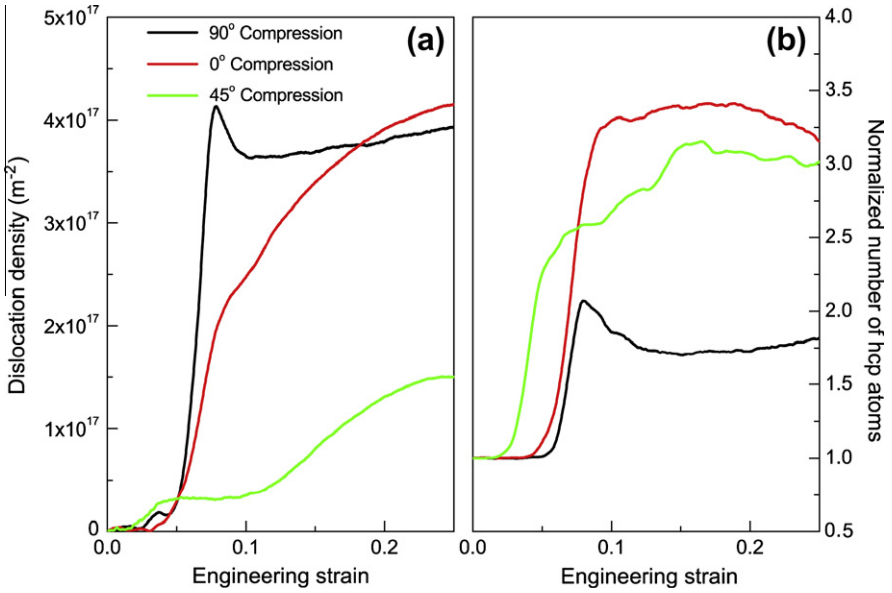

Fig. 10. Evolution of defects as the applied strain increases under different loading modes in MD simulations. (a) Dislocation density as a function of strain. (b) Variation of the normalized number of hcp atoms (by the pre-existing number) with the applied strain.

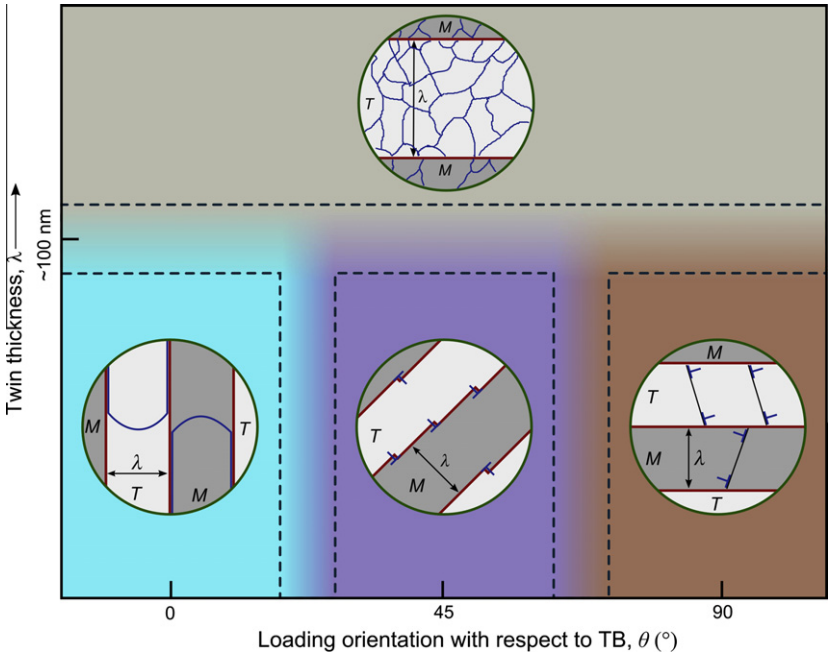

Fig. 11. Schematic illustration of a deformation-mechanism map in terms of twin thickness (λ) and loading direction (θ) with respect to TBs. There are one region corresponding to intra-twin dislocation interaction when $\lambda > \sim$100 nm and three distinct regions when $\lambda < \sim$100 nm: confined threading dislocation slip ($\theta = 0°$), partial dislocation motion induced TB migration ($\theta = 45°$), and dislocation pile-up and cutting through TBs ($\theta = 90°$).

switched by adjusting the loading direction with respect to the twin plane. The TB-mediated dislocation processes strongly influence the efficiency of TB strengthening, anisotropic yield stress and strain hardening.

To further demonstrate the twin size and orientation effects on deformation mechanisms, Fig. 12 summarizes the yield stress of nt-Cu as a function of inverse twin thickness ($1/\lambda$) from experiments and simulations. The yield strength of columnar-grained nt-Cu under 90° compression fits well to the Hall–Petch curve established by the experimental data obtained from equiaxed-grained nt-Cu [12] where dislocation pile-up also dominates. This means that the Hall–Petch strengthening ($\sigma \propto \lambda^{-1/2}$) plays a crucial role in the 90° compression. In contrast, the strength under 0° compression in this study, together with results from 0° tensile tests [14,48,49] and microhardness measurements [50,51] in the literature, all fall below the Hall–Petch curves as shown in Fig. 12. Considering the observation that the

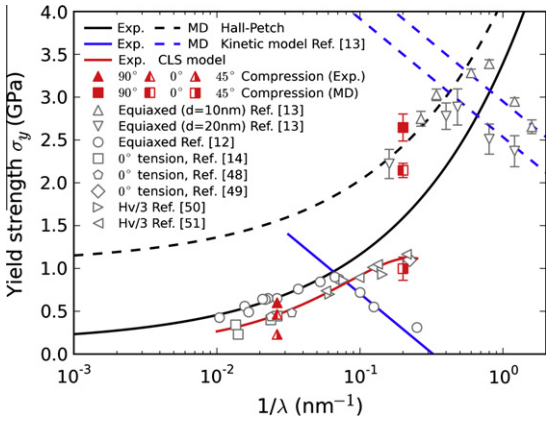

Fig. 12. Yield stress of nt-Cu (σ_y) as a function of inverse twin thickness ($1/\lambda$) showing the influence of loading directions on the efficiency of TB strengthening. For equiaxed-grained nt-Cu with λ larger than some critical value [12,13] and columnar-grained nt-Cu loaded perpendicular to TBs ($\theta = 90°$), the yield stress follows the conventional Hall–Petch relationship. In contrast, when the nt-Cu was tested parallel to TBs ($\theta = 0°$) [14,48,49] or under nanoindentation [50,51], the yield stress can be accurately described by the confined layer slip model. For the case with $\theta = 45°$, the yield stress is much lower than the other two cases. Also included are the data corresponding to TB softening in equiaxed-grained nt-Cu when λ is smaller than some critical value [12,13].

controlling deformation mechanism is switched to individual threading dislocation motion under 0° compression, the confined layer slip (CLS) model, as frequently used to model the flow stress of nanoscale thin films or multilayered materials [52,53], is adopted. Fig. 12 demonstrates that the CLS model accurately captures the variation in the yield strength of nt-Cu with twin thickness ranging from ~4.5 to ~70 nm for a loading direction parallel to TBs [14,48–51]. In the case of 45° compression, partial dislocations on the twin planes would be preferentially activated and there is almost no TB obstruction to their propagation. The flow stress in this case is expected to be controlled by dislocation nucleation at the intersections between TBs and GBs [13], with a much lower yield stress compared to the other two loading directions. Based on the three dislocation mechanisms and their different scale dependences (both mechanisms of dislocation pile-up and confined layer slip increase with twin thickness, whereas the partial-dislocation glide along TBs decreases with twin thickness), a combination of three properties of high strength, considerable ductility and strain hardening is expected in the randomly twinned Cu, as already demonstrated experimentally [6,10]. It was also observed that strength, ductility and strain hardening all increase with decreasing twin thicknesses.

5. Concluding remarks

We have identified three distinct dislocation-based deformation mechanisms in Cu with preferentially oriented nanoscale twins: namely, dislocation pile-up and slip transfer across twin boundaries, threading dislocation motion in the confined twin/matrix layers, and twin boundary migration mediated by motion of partial dislocations parallel to twin boundaries. These deformation mechanisms can be switched by simply changing the loading orientation with respect to the twin planes, resulting in the strong anisotropy in both yield strength and strain hardening. The results highlight the novel effect of spatial organization of nanostructures (e.g. the ordered alignment of nanoscale twin lamellae in this work) on their mechanical behavior, and point to the possible means of tailoring the nanostructure and loading in order to optimize the mechanical properties of engineering materials.

Acknowledgements

L.L. acknowledges financial support by NSFC (Grants Nos. 50890171 and 51071153) and the National Basic Research Program of China (973 Program, 2012CB932202) and MOST International S&T Cooperation project of China (2010DFB54010), and the Danish National Research Foundation and the National Natural Science Foundation of China (Grant No. 50911130230) for the Danish-Chinese Center for Nanometals. L.L. and T.Z. are supported by the CAS/SAFEA international partnership program. X.L. and H.G acknowledge financial support by National Science Foundation through Grant CMMI-1161749 and the MRSEC Program (award No. DMR-0520651) at Brown University. The MD simulations were performed on TeraGrid resources (Kraken Cray XT5) provided by NICS under award No. MSS090046. Helpful discussions with J.D. Embury, N. Hensen, X.X. Huang and W. Grethe are gratefully acknowledged. T.Z. acknowledges the support by NSF Grants CMMI 0653769 and 0758265. The authors are grateful to Mr. S. Jin for sample preparation.

Appendix A. Crystal plasticity modeling

A rate-dependent, large deformation-based crystal plasticity model was used to simulate the stress–strain behaviors in nt-Cu [54]. A polar decomposition of deformation gradient $\mathbf{F}$ was taken as $\mathbf{F} = \mathbf{F^e F^p}$, where $\mathbf{F}^e$ and $\mathbf{F}^p$ are the elastic and plastic deformation gradients, respectively. The rate of plastic deformation gradient $\dot{\mathbf{F}}^p$ is given by $\dot{\mathbf{F}}^p = \mathbf{L}^p\mathbf{F}^p$. Here, $\mathbf{L}^p = \sum_{i=1}^{21} \dot{\gamma}_i^p \mathbf{m}_i \otimes \mathbf{n}_i$ is the plastic rate of velocity gradient, $\dot{\gamma}_i^p$ is the plastic shearing rate on slip system i, $\mathbf{m}_i$ and $\mathbf{n}_i$ are unit vectors of the associated slip direction and slip plane normal, respectively. In the nt-Cu, the number of effective slip systems increases to 21, owing to mirror symmetry of the $\{1\,1\,1\}\langle 1\,1\,0\rangle$ slip systems inclined to TBs. A power law was used to represent the plastic shearing rate $\dot{\gamma}_i^p$ in terms of the resolved shear stress τ_i and slip resistance s_i, namely $\dot{\gamma}_i^p = \dot{\gamma}_0^p |\tau_i/s_i|^{1/m} \mathrm{sign}(\tau_i)$, where $\dot{\gamma}_0^p$ is the plastic shearing rate constant and m is the rate-sensitivity exponent of slip. The slip resistance s_i, with an initial value of s_i^0, evolves according to $\dot{s}_i = \sum_j h_{ij} |\dot{\gamma}_j^p|$. Here, h_{ij} is the rate of strain hardening on slip system i due to a

Table A1
Material parameters in crystal plasticity modeling.

C_{11} (GPa)	C_{12} (GPa)	C_{44} (GPa)	$\dot{\gamma}_0$	m	Hard I, II		Soft		h_0 (GPa)	α
					s_i^0 (MPa)	s_i^{sat} (MPa)	s_i^0 (MPa)	s_i^{sat} (MPa)		
170	124	75	10^{-3}	0.023	205	210	170	180	1	0.5

shearing on slip system j; the self-hardening rate on slip system i is $h_{ii} = h_0(1 - s_i/s_i^{sat})^{\alpha}$, where h_0, s_i^{sat} and α are hardening parameters which take different values for slip systems of hard and soft modes. The ratio of the latent hardening rate to the self-hardening rate, q, was taken as the typical value of 1.4 for fcc metals.

The above constitutive model was implemented in the finite-element simulation package ABAQUS/Explicit by writing a user material subroutine (VUMAT). The material parameters (Table A1) were determined by fitting to the experimental stress–strain data for the three loading orientations, which allowed the separate calibration of slip-resistance parameters on different slip systems of hard I, II and soft modes. Interestingly, our numerical experiments indicated that the fitted values of s_i^0 and s_i^{sat} are approximately the same for both hard I and II modes of slip, despite the different slip vectors and slip planes. This implied the same kind of the strength-controlling mechanisms (e.g. cross-slipping into the conjugate {1 1 1} slip planes) for the two hard modes of slip, which requires further atomistic study in the future. In the present finite-element simulations, each element corresponded to one single crystal, and 125 elements were used to represent random crystal orientations in the twin plane.

Appendix B. Supplementary material

Supplementary data associated with this article can be found, in the online version, at http://dx.doi.org/10.1016/j.actamat.2012.09.052.

References

[1] Courtney TH. Mechanical behavior of materials. Boston, MA: McGraw-Hill; 2000.
[2] Meyers MA, Mishra A, Benson DJ. Prog Mater Sci 2006;51:427.
[3] Lu K, Lu L, Suresh S. Science 2009;324:349.
[4] Koch CC, Morris DG, Lu K, Inoue A. MRS Bull 1999;24:54.
[5] Lu L, Shen Y, Chen X, Qian L, Lu K. Science 2004;304:422.
[6] Shen YF, Lu L, Lu QH, Jin ZH, Lu K. Scr Mater 2005;52:989.
[7] Chen XH, Lu L, Lu K. Scr Mater 2011;64:311.
[8] Zhang X, Misra A, Wang H, Shen TD, Nastasi M, Mitchell TE, et al. Acta Mater 2004;52:995.
[9] Zhang X, Misra A, Wang H, Nastasi M, Embury JD, Mitchell TE, et al. Appl Phys Lett 2004;84:1096.
[10] Chen XH, Lu L. Scr Mater 2007;57:133.
[11] Lu L, Schwaiger R, Shan ZW, Dao M, Lu K, Suresh S. Acta Mater 2005;53:2169.
[12] Lu L, Chen X, Huang X, Lu K. Science 2009;323:607.
[13] Li X, Wei Y, Lu L, Lu K, Gao H. Nature 2010;464:877.
[14] You ZS, Lu L, Lu K. Acta Mater 2011;59:6927.
[15] Dao M, Lu L, Shen YF, Suresh S. Acta Mater 2006;54:5421.
[16] Jerusalem A, Dao M, Suresh S, Radovitzky R. Acta Mater 2008;56:4647.
[17] Zhu L, Ruan H, Li X, Dao M, Gao H, Lu J. Acta Mater 2011;59:5544.
[18] Jin ZH, Gumbsch P, Ma E, Albe K, Lu K, Hahn H, et al. Scr Mater 2006;54:1163.
[19] Jin ZH, Gumbsch P, Albe K, Ma E, Lu K, Gleiter H, et al. Acta Mater 2008;56:1126.
[20] Zhu T, Gao H. Scr Mater 2012;66:843.
[21] Hazzledine PM, Kad BK. Mater Sci Eng A 1995;192–193:340.
[22] Dimiduk D, Hazzledine P, Parthasarathy T, Mendiratta M, Seshagiri S. Metall Mater Trans A 1998;29:37.
[23] Inui H, Oh MH, Nakamura A, Yamaguchi M. Acta Metall Mater 1992;40:3095.
[24] Werwer M, Cornec A. Int J Plast 2006;22:1683.
[25] Fujiwara T, Nakamura A, Hosomi M, Nishitani SR, Shirai Y, Yamaguchi M. Philos Mag A 1990;61:591.
[26] Mara NA, Bhattacharyya D, Hirth JP, Dickerson P, Misra A. Appl Phys Lett 2010;97:021909.
[27] Berendsen HJC, Postma JPM, van Gunsteren WF, DiNola A, Haak JR. J Chem Phys 1984;81:3684.
[28] Mishin Y, Mehl MJ, Papaconstantopoulos DA, Voter AF, Kress JD. Phys Rev B 2001;63:224106.
[29] Nosé S. J Chem Phys 1984;81:511.
[30] Tuckerman M, Berne BJ, Martyna GJ. J Chem Phys 1992;97:1990.
[31] Van Swygenhoven H, Farkas D, Caro A. Phys Rev B 2000;62:831.
[32] Schiotz J, Jacobsen KW. Science 2003;301:1357.
[33] Wolf D, Yamakov V, Phillpot SR, Mukherjee A, Gleiter H. Acta Mater 2005;53:1.
[34] Bunge HJ, Roberts WT. J Appl Cryst 1969;2:116.
[35] Bate P, Roberts WT, Wilson DV. Acta Metall 1981;29:1797.
[36] Kocks UF, Franciosi P, Kawai M. Text Microstruct 1991;14–18:1103.
[37] Hansen N, Jensen DJ. Acta Metall Mater 1992;40:3265.
[38] Winther G, Jensen DJ, Hansen N. Acta Mater 1997;45:2455.
[39] Taylor GI. J Inst Metals 1938;62:307.
[40] Afanasyev KA, Sansoz F. Nano Lett 2007;7:2056.
[41] Cao AJ, Wei YG, Mao SX. Appl Phys Lett 2007;90:151909.
[42] Shabib I, Miller RE. Acta Mater 2009;57:4364.
[43] Stukowski A, Albe K, Farkas D. Phys Rev B 2010;82:224103.
[44] Field DP, True BW, Lillo TM, Flinn JE. Mater Sci Eng A 2004;372:173.
[45] Wang YB, Sui ML, Ma E. Philos Mag Lett 2007;87:935.
[46] Froseth A, Van Swygenhoven H, Derlet PM. Acta Mater 2004;52:2259.
[47] Li L, Ghoniem NM. Phys Rev B 2009;79:075444.
[48] Merz MD, Dahlgren SD. J Appl Phys 1975;46:3235.
[49] Zhang X, Wang H, Chen XH, Lu L, Lu K, Hoagland RG, et al. Appl Phys Lett 2006;88:173116.
[50] Anderoglu O, Misra A, Wang H, Ronning F, Hundley MF, Zhang X. Appl Phys Lett 2008;93:083108.
[51] Anderoglu O, Misra A, Wang H, Zhang X. J Appl Phys 2008;103:094322.
[52] Nix W. Metall Mater Trans 1989;A20:2217.
[53] Misra A, Hirth JP, Hoagland RG. Acta Mater 2005;53:4817.
[54] Kalidindi SR, Bronkhorst CA, Anand L. J Mech Phys Solid 1992;40:537.